

Electronic Supplementary Material (ESI) for Journal of Materials Chemistry C.
This journal is © The Royal Society of Chemistry 2020

Supporting Information

The frequency-response behaviour of flexible piezoelectric devices for detecting the magnitude and loading rate of stimuli

Ye Qiu,^{a,b} Shenshen Sun,^{a,b} Cong Xu,^{a,b} Youyan Wang,^{a,b} Ye Tian,^{*a,b} Aiping Liu,^{*c} Xu Hou,^d Hao Chai,^e Zheng zhang,^{a,b} and Huaping Wu,^{*a,b}

^aCollege of Mechanical Engineering, Zhejiang University of Technology, Hangzhou 310023, China.

^bKey Laboratory of Special Purpose Equipment and Advanced Processing Technology, Ministry of Education and Zhejiang Province, Zhejiang University of Technology, Hangzhou 310023, China.

^cCenter for Optoelectronics Materials and Devices, Zhejiang Sci-Tech University, Hangzhou 310018, China.

^dDepartment of Engineering Mechanics, School of Aeronautics and Astronautics, Zhejiang University, 310027 Hangzhou, China.

^eZhijiang College of Zhejiang University of Technology, Shaoxing 312030, China

^{*a,b} E-mail: tianye@zjut.edu.cn; wuhuaping@gmail.com.

^{*c} E-mail: liuaiping1979@gmail.com

Table of context:

- S1.** The experimental setup for the piezoelectric signal and force measurement
- S2.** Characterization of piezoelectric properties of P(VDF-TrFE) and BaTiO₃ composite films
- S3.** SEM images of P(VDF-TrFE) and BaTiO₃ composite films
- S4.** Comparison of the phase shift between the piezoelectric voltage and loading force
- S5.** Relationship between output voltage and loading (bending) rate
- S6.** Bending strain rate sensing capability of the piezoelectric sensor attached on the wing of the bionic flying robots
- S7.** The experimental setup 3D scanner (PD13D) for verifying the accuracy of strain and strain rate detected by the piezoelectric sensor

S1. The experimental setup for the piezoelectric signal and force measurement

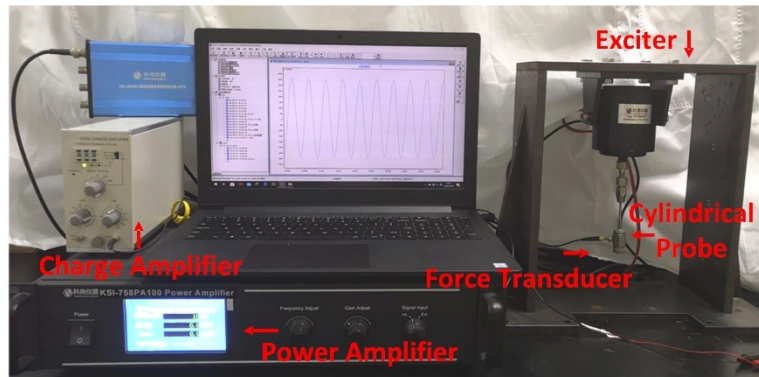


Fig. S1. The experimental setup for the piezoelectric signal and force measurement

S2. Characterization of piezoelectric properties of P(VDF-TrFE) and BaTiO₃ composite films

X-ray diffraction (XRD) is conducted to provide a more comprehensive phase characterization of P(VDF-TrFE) films and BaTiO₃ nanoparticles, as shown in Fig. S2a. The results demonstrate that the diffraction peak at 19.9°, corresponding to the overlapping of (110) and (200) reflections, is attributed to the β phase of P(VDF-TrFE) films.^[1,2] Meanwhile, BaTiO₃ nanoparticles have eight diffraction peaks ((1 0 0), (1 1 0), (1 1 1), (2 0 0), (2 1 0), (2 1 1), (2 2 0) and (2 2 1)).^[3,4] Both of the characteristic diffractions for P(VDF-TrFE) and BaTiO₃ are also observed in the profiles of nanocomposite films with 0-20 wt% of BaTiO₃ nanoparticles with respect to P(VDF-TrFE).

In addition, FTIR technology is used to characterize the transition from α phase to β phase in the nanocomposite, and the spectra is displayed in Fig. S2b. The peak at 763 cm⁻¹ is the bending vibration and skeletal mode peak of CF₂, which is suggested to be the characteristic absorption of α -phase. The peak at 837 cm⁻¹ is the rocking vibration peak of CH₂, the asymmetric stretching vibration of CF₂ and C-C skeleton vibration peak, which is assigned to the unique peak

of β -phase.^[5] In order to quantitatively study the content of β -phase, we estimated the relative β phase content of the samples according to the formula

$$F(\beta) = \frac{X_{\beta}}{X_{\alpha} + X_{\beta}} = \frac{A_{\beta}}{(K_{\beta} / K_{\alpha})A_{\alpha} + A_{\beta}} \quad (1)$$

where A_{α} and A_{β} are the characteristic absorption areas of α phase at 763 cm^{-1} and β phase at 837 cm^{-1} , respectively; K_{α} and K_{β} are the absorption coefficients of $6.1 \times 10^4 \text{ cm}^2/\text{mol}$ for α phase and $7.7 \times 10^4 \text{ cm}^2/\text{mol}$ for β phase at the corresponding wavelengths. The relative fractions of β phase for P(VDF-TrFE) nanocomposite films are illustrated in Fig. S2c. It can be observed that the β -phase fraction $F(\beta)$ increases due to the addition of BaTiO_3 nanoparticles, and reaches a maximum of 98 % in 10 wt% nanocomposite. The results illustrate that the BaTiO_3 nanoparticles in nanocomposite acting as the heterogeneous nucleation agent, which is beneficial to the crystallization of macromolecular chains.

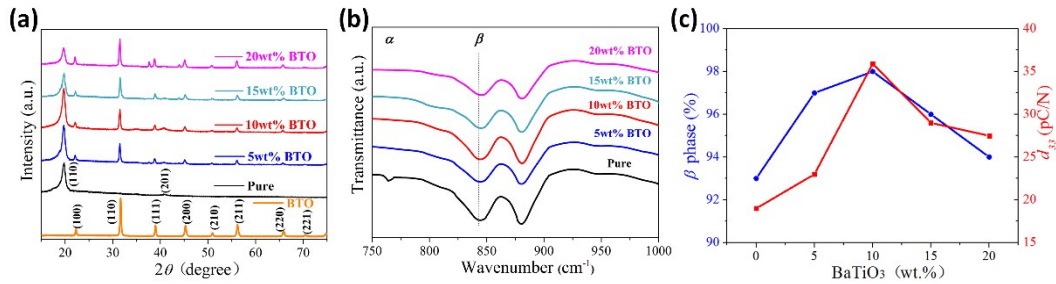


Fig. S2. (a) The XRD, (b) FTIR spectrum and (c) piezoelectric coupling coefficient d_{33} results of P(VDF-TrFE) and BaTiO_3 composite films.

All the above results indicate that the P(VDF-TrFE) matrix has a high β phase crystallinity. In order to reflect piezoelectric performance more intuitively, Fig. S2c also shows the piezoelectric coupling coefficient d_{33} values of nanocomposite films. The d_{33} values of pure P(VDF-TrFE) film and P(VDF-TrFE) with 10 wt% BaTiO_3 composite are 19 and 35.9 pC N^{-1} , respectively. All

these results show the BaTiO₃ nanoparticles significantly enhance the piezoelectric performance of the nanocomposite material.

S3. SEM images of P(VDF-TrFE) and BaTiO₃ composite films

Furthermore, the representative morphologies of P(VDF-TrFE) and BaTiO₃ composites are shown in Fig. S3. The magnified scanning electron microscopy (SEM) images show the uniform distribution of composites, which reveals excellent interfacial adhesion between BaTiO₃ particles and the P(VDF-TrFE) matrix. On gradually increasing the weight fraction of BaTiO₃ from 0 to 20 wt%, it results in a correspondingly increase of the distribution density of piezoelectric ceramic particles.

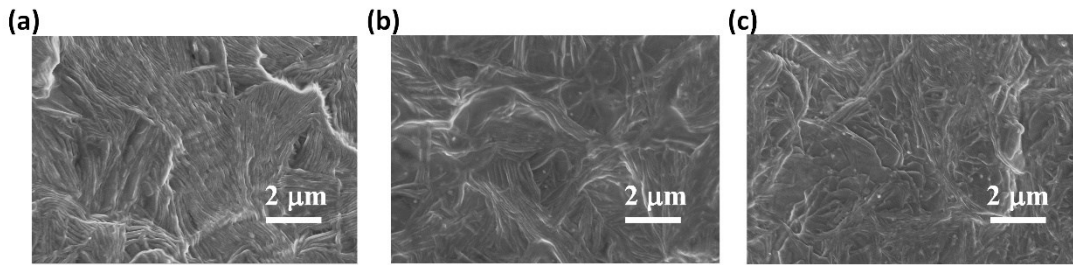


Fig. S3. SEM images of P(VDF-TrFE) and 100 nm BaTiO₃ composites with different BaTiO₃ filler loadings of (a) 0 wt%, (b) 10 wt%, (c) 20 wt%.

S4. Comparison of the phase shift between the piezoelectric voltage and loading force

The phase shift between the piezoelectric voltage and loading force with the loading frequency of 100 Hz (Fig. S4a) shows the peak value of the voltage is before the peak value of the force, which is attributed to the incomplete collection of the piezoelectric charge. Although the loading pressure continues, the free-charge carriers have already return across the external circuit, giving rise to a negative peak. Meanwhile, the periods of voltage measurement is larger than the loading time, resulting in a complete loading in the high-frequency loading. Thus, the voltage peak value is after the pressure peak value as shown in Fig. S4b.

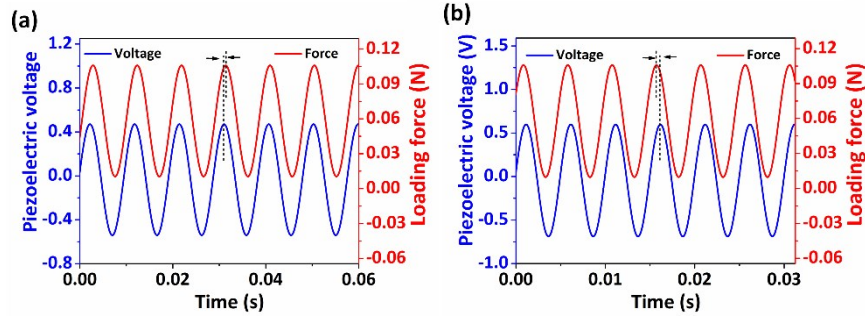


Fig. S4. Comparison of the phase shift between the piezoelectric voltage and loading force. (a) The phase shift between piezoelectric voltage and loading force with the loading frequency of 100 Hz. (b) The phase shift between voltage and force with the loading frequency of 200 Hz.

S5. Relationship between output voltage and loading (bending) rate

The loading rate r_{loading} is related to the pressure F and frequency f by

$$r_{\text{loading}} = F_{\text{max}} / (0.5 \times T) = 2F_{\text{max}}f, \text{ where } r_{\text{loading}} \text{ is loading strain rate, } F_{\text{max}} \text{ is maximum compressive force,}$$

T is period, and f is frequency. The $F = F_{\text{max}} [1 - \cos(2\pi ft)] / 2$ can be rewritten as

$$F = F_{\text{max}} [1 - \cos(4\pi F_{\text{max}} t / r_{\text{loading}})] / 2. \text{ The voltage } V = \frac{(-e)l}{k} \frac{F}{AE} - \frac{(-e)l^2}{AR(k)^2} \int_0^t \frac{F}{A(E)} e^{\frac{lt}{ARk}} dt \text{ is expressed as:}$$

$$V = \frac{(-e)l}{k} \frac{F_{\text{max}} [1 - \cos(4\pi F_{\text{max}} t / r_{\text{loading}})] / 2}{AE} - \frac{(-e)l^2}{AR(k)^2} \int_0^t \frac{F_{\text{max}} [1 - \cos(4\pi F_{\text{max}} t / r_{\text{loading}})] / 2}{A(E)} e^{\frac{lt}{ARk}} dt. \quad (2)$$

Meanwhile, the bending rate r_{bending} is related to the strain ε and frequency f by

$$r_{\text{bending}} = \varepsilon_{\text{max}} / (0.5 \times T) = 2\varepsilon_{\text{max}}f. \text{ The voltage } V = \frac{(-e)l}{k} \frac{\varepsilon}{AE} - \frac{(-e)l^2}{AR(k)^2} \int_0^t \frac{\varepsilon}{A(E)} e^{\frac{lt}{ARk}} dt \text{ can be rewritten as:}$$

$$V = \frac{(-e)l}{k} \frac{\varepsilon_{\text{max}} [1 - \cos(4\pi \varepsilon_{\text{max}} t / r_{\text{bending}})] / 2}{AE} - \frac{(-e)l^2}{AR(k)^2} \int_0^t \frac{\varepsilon_{\text{max}} [1 - \cos(4\pi \varepsilon_{\text{max}} t / r_{\text{bending}})] / 2}{A(E)} e^{\frac{lt}{ARk}} dt. \quad (3)$$

S6. Bending strain rate sensing capability of the piezoelectric sensor attached on the wing of the bionic flying robots

The bending strain rate of the wing of a bionic bee can be determined from the piezoelectric signal, since it scales linearly with the peak of the piezoelectric pulse. Because the calibrated slope is 0.011 V/(%/s) (Fig. S6), the linear relationship is expressed as $V = r \times 0.011$. The measured V of 0.26 V, 0.45V, and 0.71 then gives a bending rate of 24 %/s, 46 %/s and 95 %/s.

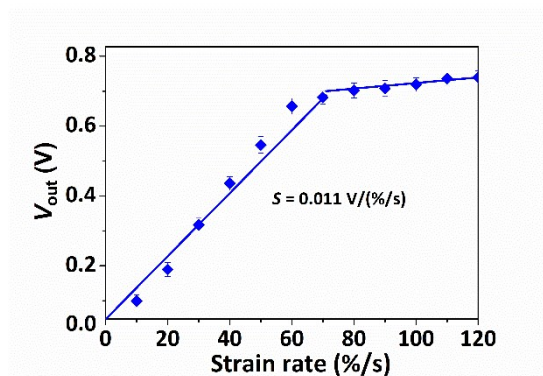


Fig. S6. Bending strain rate sensing capability of the piezoelectric sensor attached on the wing of the bionic flying robots.

S7. The experimental setup 3D scanner (PD13D) for verifying the accuracy of strain and strain rate detected by the piezoelectric sensor

The 3D scanner (PD13D) has been used to verify the accuracy of the strain rate and strain (Fig. S7), and the average relative error is controlled within 10%. Firstly, reference points are pasted on the surface of the wing to assist in coordinate transformation during multi-view scanning. Importing the data after scanning into Geomagic post-processing software to obtain the coordinates of each point of the wing. Finally, the strain is calculated by MATLAB through the coordinate position of three points on the section, and the strain rate is obtained by combining the deformation time.



Fig. S7. The experimental setup 3D scanner (PD13D) for verifying the accuracy of strain and strain rate detected by the piezoelectric sensor.

References

- [1] V. Cauda, S. Stassi, K. Bejtka, G. Canayese, *ACS Appl. Mater. Inter.* 2013, **5**, 6430-6437.
- [2] K. Lau, Y. Liu, H. Chen, R. L. Withers, *Adv. Cond. Matter. Phys.*, 2013, **2013**, 435938.
- [3] X. L. Chen, X. M. Li, J. Y. Shao, N. L. An, H. M. Tian, C. Wang, T. Y. Han, L. Wang, B. H. Lu, *Small*, 2017, **13**, UNSP 1604245.
- [4] M. H. Bi, Y. A. Hao, J. M. Zhang, M. Lei, K. Bi, *Nanoscale*, 2017, **9**, 16386.
- [5] A. C. Wang, Z. Liu, M. Hu, C. C. Wang, X. D. Zhang, B. J. Shi, Y. B. Fan, Y. G. Cui, Z. Li, K. L. Ren, *Nano Energy*, 2018, **43**, 63.